Local Resolution Adaptation for Curved Slice Echo Planar Imaging

Hans Weber[1], Jakob Assländer[1], Sebastian Littin[1], Jürgen Hennig[1], and Maxim Zaitsev[1]
[1]*Department of Radiology, Medical Physics, University Medical Center Freiburg, Freiburg, Germany*

Introduction

The ExLoc technique [1] allows for an adaptation of the slice shape to the anatomy under investigation based on a set of adjustable nonlinear magnetic encoding fields (Fig. 1). ExLoc is in particular promising for functional MRI experiments, as the technique would not only allow for an increased sampling rate of the BOLD signal, due to an improved coverage of the relevant volume with fewer slices, but also separate loci activation could be simultaneously selected for synchronized data acquisition. As demonstrated already [2], application of ExLoc to echo planar imaging (ExLoc EPI) for acquisition of the BOLD signal in a curved slice is feasible. However, as the experiments also revealed, the natural variation in image resolution caused by the fields' nonlinearity becomes in particular a problem for these lower resolved acquisitions, as important anatomical structures may not be resolved. The local FOV technique [3] allows for a compensation of the variation in voxel size by locally adapting the image resolution. As shown recently [4], the technique is applicable to curved-slice imaging with robust sequences such as gradient echo (GRE). However, it is questionable, whether this still holds true for sequences with continuous trajectories such as EPI, which is typically affected by image distortions resulting from their high sensitivity to B_0 inhomogeneities.

Within this study, we explore the applicability of the local FOV technique to in vivo ExLoc EPI with the final goal of achieving a more homogenous resolution in curved slice functional imaging. For comparison, the technique is also applied to GRE imaging with equal resolution.

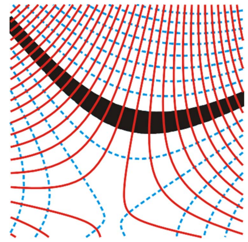

Fig. 1: Isocontours of an ExLoc slice selection field (blue), the corresponding encoding field (red) and a cross-section of the selected slice (black)

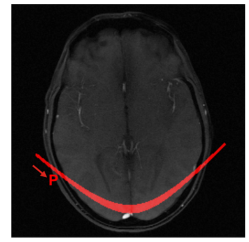

Fig. 2: Localizer image of the *xy*-plane, showing a cross-section of the selected slice. The slice exhibits no variation along the *z*-dimension

Methods

The local FOV technique exploits a unique property of encoding with nonlinear fields that causes k-space samples to have a spatially localized contribution to the reconstruction of the object. The technique is based on the assumption of a constant level of object detail. Due to the spatial variation of image resolution, this level of object detail is fully resolved only in a part of the FOV, with its size and location given by the particular resolution variation. To resolve the object in the remaining part (the 'local FOV'), additional, higher frequency k-space samples are required. However, as these additional samples effectively only contribute to the local FOV, they can be undersampled without introducing aliasing inside the local FOV. Iterative application of this undersampling scheme allows to further split up the local FOV, thus dividing the FOV into multiple sub-FOVs. The final k-space pattern is given by the combination of the sub-patterns of the individual sub-FOVs.

All imaging experiments were performed on a 3T MAGNETOM Trio TIM system (Siemens, Erlangen, Germany), equipped with a PatLoc gradient insert [5]. The five available magnetic field components (x, y, z, 2xy, x^2-y^2) offer encoding fields for slices with one curved dimension lying in the *xy*-plane. A curved slice was adjusted to the visual cortex of a healthy volunteer and imaged after ethics approval (Fig. 2, $FOV_{R/P}$: 207 mm/205 mm, slice thickness $_{min/max}$: 2.5 mm/7.7 mm). For this particular slice position, the encoding field variation along the curved slice dimension (P) was determined and served as basis for the calculation of the k-space sampling pattern for a total of four sub-FOVs. The final pattern consisted of 102 k-space lines with 102 points each. As a reference, an equidistantly sampled k-space pattern with the equal number of lines and points per line was designed. The k-space trajectories for the EPI acquisitions (TR: 1000 ms, TE_{eff}: 65 ms, FA: 90°, dwell time: 5 µs) were directly derived from the corresponding sampling patterns. For the GRE acquisitions (TR: 100 ms, TE: 20 ms, FA: 15°), an equidistantly sampled k-space including all desired k-space lines was acquired. Within the individual reconstruction of each sub-FOV, the corresponding k-space lines were extracted from the acquired data, distributed on an equidistant grid, zero filled and density corrected prior to Fourier transformation. For the EPI acquisitions, frequency offset compensation was applied by multiplying a phase ramp to the time domain data. The total FOV was composed from the sub-FOVs in encoding space and transformed into the final object space as described in [1].

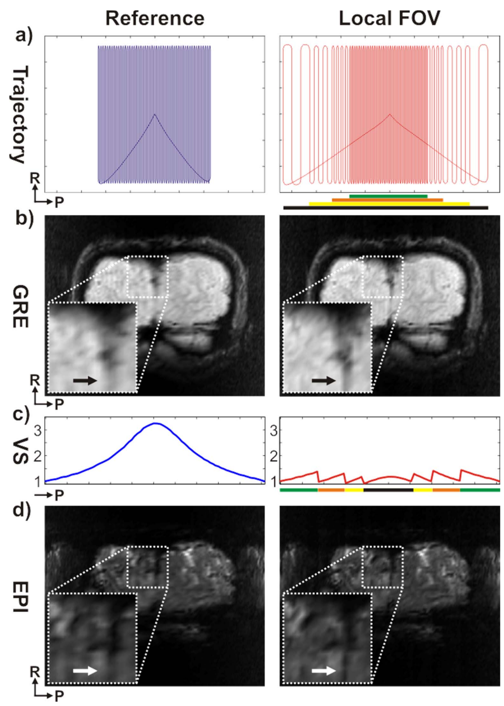

Fig. 3a: EPI trajectory for both the reference (**left**) and the local FOV acquisition (**right**) with equal number of k-space lines. **b:** Within the GRE images, the local FOV technique allows a compensation of the natural variation in image resolution by increasing the image resolution towards the center. **c:** The relative variation in voxel size (VS) shows that the compensation is achieved by adaption of the voxel size in each sub-FOV. The color-coding indicates the allocation to the k-space sub-patterns (a). **d:** Also for EPI, the local FOV technique allows to achieve a local resolution adaption for improved resolvability of the border between the hemispheres.

Results and Discussion

Figure 3 shows the results for both the reference (left) and the local FOV technique (right). The plotted EPI k-space trajectories (a) reveal the distribution of the individual k-space lines, the color-coding indicates the allocation to the individual sub-patterns. Within the GRE (b) reference image, the border between the two hemispheres vanishes (arrow), as the image resolution decreases towards the center. With the local FOV technique applied, the decrease in image resolution is compensated, thus revealing the border despite the fact that the same number of k-space lines was used. This is in accordance with the calculated relative variation in voxel size along the curved dimension (c), which yields for the reference a 3x greater voxel size in the FOV center than at the periphery. With local resolution adaptation, the natural variation in voxel size is still present, but its strength is adapted in each sub-FOV, resulting in a much more homogeneous resolution. The color-coding under the plot indicates the size and location of the individual sub-FOVs. Also for EPI (d), the local FOV technique allows to improve the image resolution towards the center. The enhancement of the uncorrected N/2 ghosting towards the FOV periphery results from the intensity correction, which is applied to compensate for both the varying in-plane voxel size and the varying slice thickness. The applied global frequency-offset compensation was essential for a successful resolution adaptation. For stronger distortions, the local FOV technique is expected to fail, as the contributions from the various sub-FOVS no longer match due to differences in local distortions. A further improvement of the technique's performance is expected by an extended distortion correction based on a B_0 inhomogeneity map. However, currently it is still an open question, how such a correction can be integrated in the local FOV framework. It is further complicated for EPI due to the fact that single-shot trajectories are additionally sensitive to trajectory deviations resulting from effects such as eddy currents, small timing imperfections, or concomitant fields. Based on these constraints, the presented pilot experiments performed better than expected, thus motivating to investigate these issues in more detail.

References [1] Weber et al., MRM 2013, 69:1317; [2] Weber et al., Proc. ISMRM 2011, #2052; [3] Weber et al., MRM 2013, doi: 10.1002/mrm.24754; [4] Weber et al., Proc. ISMRM 2013, #124; [5] Welz et al., CMRB 2013, 43:111;

Acknowledgement This work was supported by the European Research Council Starting Grant 'RANGEMRI', grant agreement 282345 and Advanced Grant 'OVOC', grant agreement 232908.